論文 / 著書情報
Article / Book Information

Title	Experimental analysis of the sweepback angle effect on the thrust generation of a robotic penguin wing
Authors	Yayi Shen, Hiroto Tanaka
Citation	Bioinspiration & Biomimetics, Vol. 18, Issue 2,
Pub. date	2023, 2
DOI	https://doi.org/10.1088/1748-3190/acb521
Copyright	This is the Accepted Manuscript version of an article accepted for publication in Bioinspiration & Biomimetics. IOP Publishing Ltd is not responsible for any errors or omissions in this version of the manuscript or any version derived from it. The Version of Record is available online at https://doi.org/10.1088/1748-3190/acb521.
Note	This file is author (final) version.

Experimental Analysis of the Sweepback Angle Effect on the Thrust Generation of a Robotic Penguin Wing

Yayi Shen[1] and Hiroto Tanaka[2†]
[1]College of Mechanical & Electrical Engineering, Nanjing University of Aeronautics and Astronautics, Nanjing, China
[2]Department of Mechanical Engineering, Tokyo Institute of Technology, Tokyo, Japan
[†]Author for correspondence: HT, tanaka.h.cb@m.titech.ac.jp
ORCID iDs: YS, 0000-0002-0866-5256; HT, 0000-0003-4233-8918

Abstract—Penguins have evolved excellent swimming skills as diving birds, benefiting from their agile wings. This paper experimentally analyses the effect of the wing sweepback angle on thrust generation using a robotic penguin wing. A developed wing mechanism that can realize penguin-like flapping and feathering motion was employed for actuating five alternative wing models with different sweepback angles from 0° to 50°. Force measurements under a steady water flow were conducted for both fixed and flapping states for all wing models. The results showed that small sweepback angles of 30° or less in the fixed state led to a steep lift curve and that a moderate sweepback angle of 30° produced the largest lift-to-drag ratio. In the flapping state, the smaller-sweepback wings generated a larger net thrust for the same wing motion, whereas the larger-sweepback wings produced more thrust given the same Strouhal number. It was also found that larger-sweepback wings more easily achieved the maximum net thrust in terms of less angle-of-attack control. On the other hand, the hydrodynamic efficiency was not greatly affected by the sweepback. Regardless of the sweepback, the trend of the efficiency increasing with increasing flow speed indicated that the penguin wings can be more suitable in high-speed locomotion for higher hydrodynamic efficiency.

Keywords: sweepback angle, penguin wing, robotic penguin, thrust generation, aquatic locomotion

1. Introduction

Biomimetic swimming robots have been verified to deliver high energy efficiency as well as favourable dynamic characteristics and noiseless motion [1]–[4]. In recent decades, researchers have been dedicated to improving the performance of biomimetic underwater robots from various aspects [5]–[13]. To explore how the fish fin shape affects thrust performance, Kikuchi et al. classified the morphological shape of fish fins into polygonal shapes and compared the shapes through experiments [6]. Feilich and Lauder revealed that the fin shape interacts with the flexural stiffness in complicated ways to produce swimming performance [7]. Given that the stiffness varies in real fish bodies, Lucas et al. identified the role of nonuniform bending stiffness during fish propulsion [8], and Zhong et al. developed a tuna-like robot with a tail of tunable stiffness to enable fast and efficient swimming [9]. While earlier studies mainly focused on imitating the morphology and kinetics of fish, other aquatic animals possessing efficient swimming skills have drawn people's attention recently, such as sea lions [14], water beetles [15] and even humans [16].

In our research, we focus on the thrust generation of a penguin-mimetic flapping-wing mechanism. Penguins are diving birds that inhabit the Southern Hemisphere. During evolution, they lost their ability to fly in the air and adapted to underwater swimming and foraging in the ocean. Recent video logging of wild gentoo penguins (*Pygoscelis papua*) revealed that the penguins perform precise hit-and-run attacks on small prey or actively pursue large prey owing to their mobility [17]. A satellite tracking study of the Fiordland penguin (*Eudyptes pachyrhynchus*) reported that the maximum daily travel distance can be more than 200 km [18]. These excellent swimming performances have motivated us to explore the relation between wing motion and the generated propelling forces. In our previous work, the 3-D wing motion of a real penguin during swimming was measured in an aquarium [19], and a robotic penguin wing was developed to mimic the motion [20]. Based on the measurement, we defined the wing motion and decomposed it into three degrees of freedom: flapping, feathering and pitch of the flapping axis. Specifically, flapping is the main oscillating motion, which generates major propelling thrusts; feathering is the rotational motion of the wing along the spanwise direction, which adjusts the angle of attack (AoA) and boosts the thrust; and pitch is characterized by the direction of the flapping plane, thus affecting the direction of the thrust. In contrast to other swimming animals that use an oscillating mechanism for propulsion, we notice that they seldom can realize such agile motions at the same time with only one propulsor (wing/fin/tail). For example, cetacean flukes are largely responsible for the generation of thrust, while the other control surfaces are the pectoral flippers, dorsal fin, and caudal peduncle [21]. A developed dolphin robot also generated the main thrust with the fluke and used the pectoral fins for balance control [22]. The ability of the robotic penguin wing to effectively control the thrust magnitude by active feathering and the thrust direction by variation in pitch has been verified.

However, the wing model that we fabricated for the previous study was a no-sweepback wing, which means that the leading edge of the wing is set to be vertical to the longitudinal axis of the body. During our observations on the swimming of real penguins, it was found that the wings swept backwards by a range from 24.6° to 46.7° relative to the forward direction [19]. This variation in the sweepback angle possibly affects the thrust and efficiency of the flapping-wing propulsion. In fact, our CFD (computational fluid dynamics) simulations of fixed wings with a realistic penguin wing model showed that the lift and drag coefficients of the wings change with the sweepback and that drag can be reduced by sweepback for a constant lift [23]. Therefore, it is important to investigate the effect of the sweepback on thrust generation by flapping for both the development of penguin-mimetic robots and the understanding of the biomechanics of penguin swimming.

The geometric feature of sweepback has also been observed in the fins of fish [24], [25], flippers of aquatic animals [26], and wings of flying birds or insects [27], [28]. Recently, Zurman-Nasution et al. conducted CFD simulations of penguin-like flapping wings with a simplified wing model, reporting that the sweepback slightly decreases thrust and efficiency [29]. In this paper, we experimentally investigated the effect of sweepback on thrust generation by flapping with a realistic penguin wing model. Five wing models with different sweepback angles were employed for comparison. First, the lift and drag coefficients of all the wings that were fixed in steady flow were measured in a water tunnel to obtain the static wing characteristics. Then, the propelling thrust and the hydrodynamic efficiency during flapping motions were measured and analysed for flapping in steady flow.

The remainder of this paper is organized as follows. The design of the robotic wing mechanism, method of quasisteady hydrodynamic calculations, and experimental procedure for fixed- and flapping-wing cases are introduced in Section 2. Section 3 presents the measured and calculated results. Finally, conclusions are stated in Section 4.

2. Materials and methods

2.1. Wing mechanism

To achieve wing motions similar to those realized in real penguins, a 3-DoF robotic penguin wing has been developed [20]. In this paper, only the flapping and feathering motions are involved to vary the thrust magnitude, while the flapping axis is parallel to the flow of a water tunnel. Fig. 1(a) schematically shows the flapping and feathering motions realized by the penguin wing. The flapping axis is parallel to the longitudinal direction of the body. The feathering axis is parallel to the spanwise direction and perpendicular to the flapping axis. By actively controlling feathering, the AoA between the wing and the relative flow velocity can be adjusted. Fig. 1(b) and (c) illustrate how the two motions are achieved by utilizing a differential gear system. The mechanism contains three identical bevel gears. Opposing bevel gears 1 and 2 are actively controlled by two servo motors (KRS-4032HV, KONDO, Japan) through timing belts. Bevel gear 3 thus can be actuated to rotate around the X_W-axis and the Z_W-axis. A 3-D printed wing is connected to bevel gear 3 so that the wing can realize flapping motion (around the X_W-axis) and feathering motion (around the Z_W-axis). The rotational axes and the coordinate systems are depicted in the figure, where body frame B is fixed at the base part and the $+X_B$-axis indicates the forwards swimming direction (opposite to the flow direction of the water tunnel). The wing frame W is fixed to the wing, the X_W-axis indicates the chordwise direction, and the Z_W-axis indicates the spanwise direction, which is vertical to the robot body or the penguin body. To feedback the angular positions of both the flapping and feathering motions in real time, two potentiometers (P13SM, Vishay Intertechnology, USA) are installed as well.

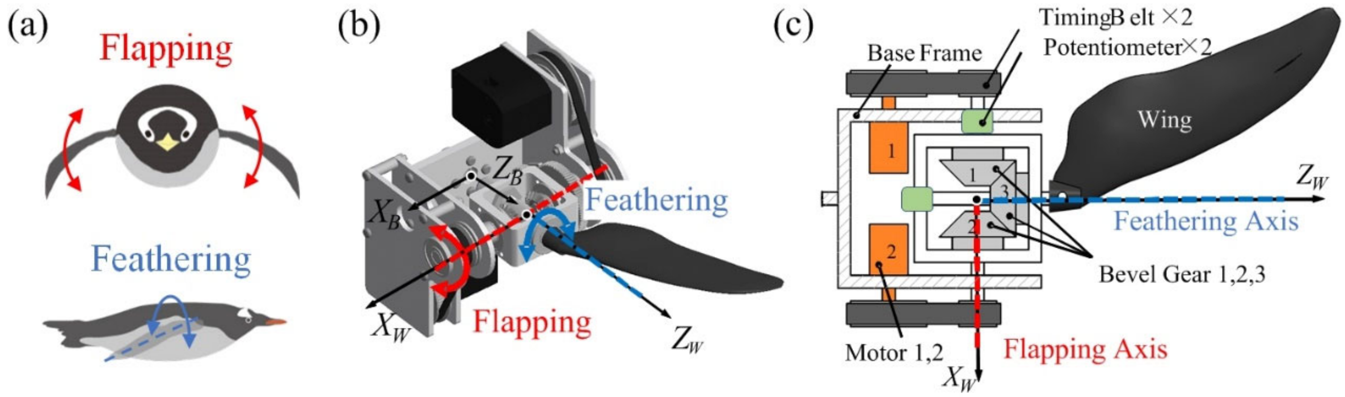

Fig. 1. (a) Flapping and feathering motion realized by the penguin wing; (b) 3-D model of the wing mechanism; (c) schematic drawing of the wing mechanism. The flapping and feathering angles are zero in schematics (b) and (c).

As shown in Fig. 2, six wing models with different sweepback angles are printed with a 3-D printer (Ultimaker S5, Ultimaker B.V., Netherlands) using a polylactic acid filament (Tough PLA, Ultimaker B.V., Netherlands). Note that the printed wings are rigid, although the real wings bend during flapping [17]. This makes it possible to focus on the relationship between the wing sweepback, wing kinematics, and resultant thrust by isolating the complexity of the wing deformation. The cross-sectional profiles of the wing are obtained by scanning a real penguin wing and adjusting it to obtain symmetric profiles along the thickness direction [20]. The details of the obtained profiles can be found in our previous paper [19]. According to our kinematic research on penguin swimming, the wing has an average sweepback angle of approximately 35° relative to the feathering axis +Z_W [19]. Hence, the sweepback angles studied in this paper are set from 0° to 50° at an interval of 10°, as depicted in Fig. 2. They are switched manually to connect with the wing mechanism as needed. Considering the following experimental design, 0.4-scale wing models are fabricated. The geometric parameters of the wing models are listed in Table 1. In addition, all the wings have the same projected wing area (S) of 2256 mm^2, the same wing length (l) of 101 mm, and the same maximum wing thickness of 6 mm. The aspect ratio (AR) is defined by AR $= l'^2/S$, where l' is the spanwise length of the wing. Wing profiles at spanwise positions of 25%, 50%, and 75% from the base are illustrated and summarized in Fig. 2 on the right side and Table 1, respectively. The geometric mean chord (c_g) of the wing is calculated through $c_g = S/l'$. A larger sweepback angle tends to increase the chords at all positions but does not affect the maximum thickness too much (within 0.25 mm variation). All the wing models weigh 8.7 grams.

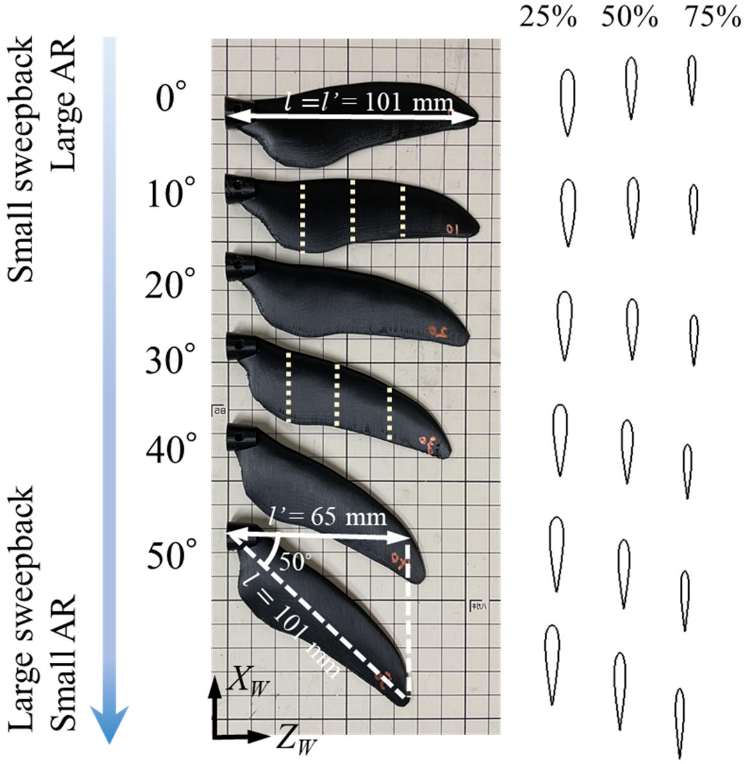

Fig. 2. 3-D printed sweepback wing models (sweepback angle from 0° to 50°) with the same wing length (*l*) but different spanwise widths (l_0) and aspect ratios (AR). Only models of 0° and 50° are marked with lengths for clarity. Wing profiles at spanwise positions of 25%, 50% and 75% from the base are depicted on the right side, which show the relative positions along two axes as well.

Table 1. GEOMETRIES OF THE SWEEPBACK WINGS

Sweepback angle (°)	Spanwise width *l'* (mm)	Aspect ratio	Chord at 25% (mm)	Chord at 50% (mm)	Chord at 75% (mm)	Mean chord (mm)	Max. thickness at 25% (mm)	Max. thickness at 50% (mm)	Max. thickness at 75% (mm)
0	101	4.5	28.59	26.65	21.43	22.3	6.00	4.67	3.23
10	99	4.3	28.69	26.00	21.45	22.8	6.00	4.71	3.29
20	95	4.0	29.74	26.19	22.10	23.7	5.97	4.75	3.30
30	87	3.4	30.79	27.30	23.51	25.9	5.93	4.79	3.35
40	77	2.6	32.09	29.49	25.96	29.3	5.89	4.83	3.40
50	65	1.9	34.16	33.14	30.09	34.7	5.85	4.86	3.47

2.2. Hydrodynamic forces of the wing

In this paper, we assume that the penguin swims straight forward, as in the directions of the $+X_B$ and $+X_W$ axes. Thus, the relation between the flow velocity ***U*** and the wing at the initial position can be depicted as shown in Fig. 3(a). We use the chords located at 75% of the spanwise ($+Z_W$-axis) length from the wing base for the following hydrodynamic analysis.

The wing profile and the cross section at the chord are shown in Fig. 3(b). Considering a moment with the flapping velocity of $\boldsymbol{v}_{flap}$, the relative inflow velocity between the flow and the flapping wing can thus be obtained through:

$$\boldsymbol{v}_{in} = \boldsymbol{U} - \boldsymbol{v}_{flap} \qquad (1).$$

The angle between the inflow velocity $\boldsymbol{v}_{in}$ and the chord line is then defined as the AoA, represented by α. The AoA is affected by the feathering angle $\theta_{feather}$. The existence of feathering reduces the AoA, and a larger feathering angle results in a smaller AoA. Specifically, the AoA can be derived through kinematics as follows:

$$\alpha = \begin{cases} \operatorname{sgn}(\theta_{feather})(\pi/2 - \arctan\dfrac{|\boldsymbol{U}|}{|\boldsymbol{v}_{flap}|} - |\theta_{feather}|), \text{ for } |\boldsymbol{v}_{flap}| \neq 0 \\ 0, \text{ for } |\boldsymbol{v}_{flap}| = 0 \end{cases} \qquad (2).$$

Thus, the AoA depends on the flapping velocity $\boldsymbol{v}_{flap}$, the feathering angle $\theta_{feather}$, and the flow velocity $\boldsymbol{U}$.

The lift and drag generated by the wing on the wing cross-section plane ($X_W Y_W$ plane) can be expressed as:

$$L = 0.5 C_L(\alpha)\rho |\boldsymbol{v}_{in}|^2 S \qquad (3),$$

$$D = 0.5 C_D(\alpha)\rho |\boldsymbol{v}_{in}|^2 S \qquad (4),$$

where L indicates the lift perpendicular to $\boldsymbol{v}_{in}$ and D indicates the drag parallel to $\boldsymbol{v}_{in}$ (Fig. 3(b)). $C_L(\alpha)$ and $C_D(\alpha)$ are the lift and drag coefficients, respectively, which are functions of the AoA; ρ represents the density of the fluid, and S is the area of the wing. $\boldsymbol{F}_W$ is a resultant force vector of L and D. Thrust F_x was defined as the forward component of $\boldsymbol{F}_W$.

In our experiment, the wing mechanism was mounted on a 6-axis force sensor. Therefore, the X_B, Y_B, and Z_B components of a total force vector $\boldsymbol{F}_B$ acting on the wing mechanism were measured by the sensor. Then, $\boldsymbol{F}_W$ was calculated as a projection of $\boldsymbol{F}_B$ on the $X_W Y_W$ plane, followed by calculation of L and D from $\boldsymbol{F}_W$. F_x is the same as the X_B components of $\boldsymbol{F}_B$. The details of the measurement setup are explained in subsection 2.4.

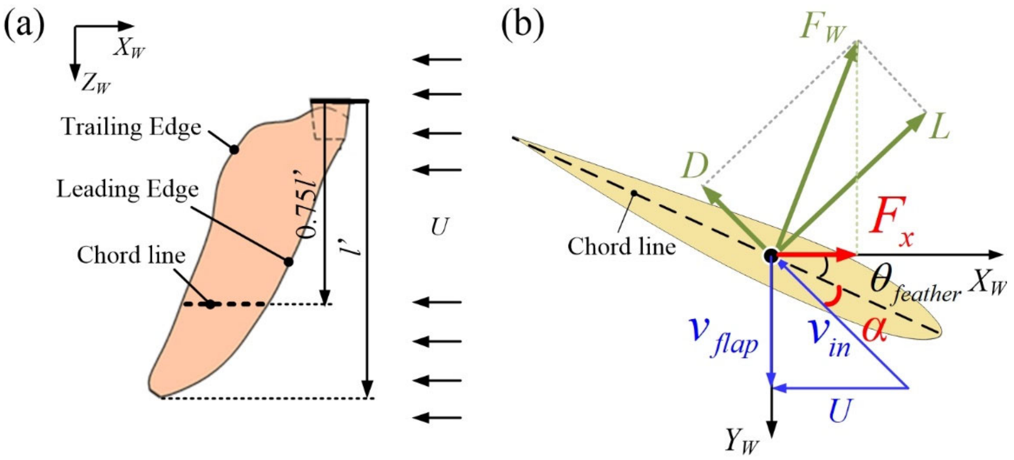

Fig. 3. (a) Representative wing chord located at 75% of the spanwise length, *l'*, from the wing base. (b) Hydrodynamic forces applied on the wing profile.

2.3. Hydrodynamic efficiency

The hydrodynamic efficiency is employed for evaluating the propulsion efficiency in the same manner as in our previous work [19], rather than the electrical efficiency, which involves mechanical consumption and specific actuators [15], [30]. The hydrodynamic efficiency is defined as:

$$\eta_{\text{hydrodynamic}} = \frac{\bar{P}_{thrust}}{\bar{P}_{hydrodynamic}} = \frac{\int_0^T F_x(t)\left|\boldsymbol{U}\right|dt}{\int_0^T \boldsymbol{F}_B(t)\cdot \boldsymbol{v}_{in}(t)dt} \qquad (5)$$

where $\bar{P}_{thrust}$ is the cycle-averaged propulsive power in the flow direction, $\bar{P}_{hydrodynamic}$ is the cycle-averaged hydrodynamic power and the inflow velocity is calculated through Equation (1).

2.4. Experimental methods

The experimental apparatus is designed for fixed-wing and flapping-wing tests of different wing models, as explained below.

a) Experimental apparatus: A force measurement setup is built as shown in Fig. 4. The fabricated wing mechanism is fixed to a 6-axis force/torque sensor (SFS080F500M5, Leptrino, Japan) suspended over a water tunnel through a steel support. The water tunnel (PT-100-Modified, West Japan Fluid Engineering Laboratory, Japan) is 1 m long, 0.3 m broad, and 0.2 m deep and offers tuneable flow speeds with a maximum value of 2 m/s. It is experimentally verified that the distances from the wing to the side and bottom walls are not sufficient to affect the results of the force measurement. The inertial frame is depicted at the bottom right of Fig. 4. The inflow velocity of the water tunnel points along the -X_0-axis, and the assumed forward swimming direction is along the +X_0-axis based on the setup of the wing mechanism. Note that there is a rotation stage connected between the force sensor and the steel support, which is used to adjust the initial direction of the wing relative to the flow direction. When the rotation stage is at its initial position, the +X_0-axis and +Z_0-axis align with the +X_B-axis and +Z_B-axis of the body frame, respectively.

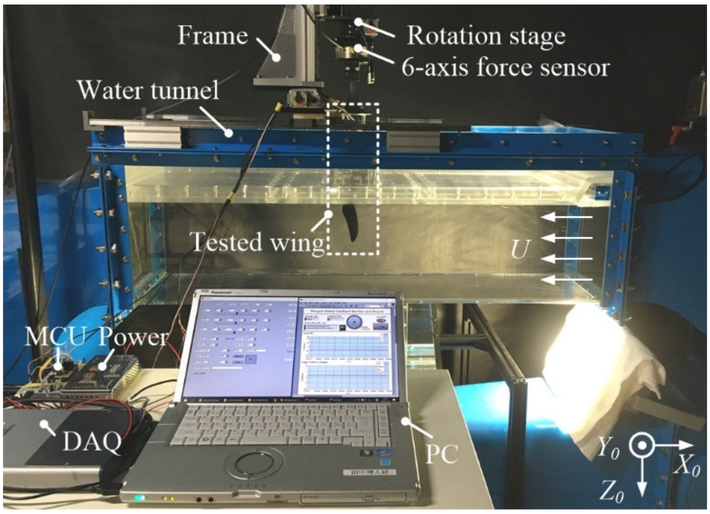

Fig. 4. Force measurement setup.

The electronic system mainly includes a master control PC, a microcontroller unit (MCU) and a data acquisition (DAQ) device. The PC working at a 64-bit Windows operation system provides high-level commands such as flapping and feathering angles, which are then converted into joint inputs through kinematic or inverse kinematic analysis. The joint inputs are then sent to the MCU (Nucleo-144, STMicroelectronics, Switzerland) to actuate the wing mechanism through a

PID controller. To record the force from the force sensor and the angular positions of the two motions from the potentiometers, a DAQ device (NI USB-6343, National Instruments, USA) working at a sampling frequency of 1000 Hz is used. In addition, the motors in the wing mechanism are powered by a 12 V constant voltage source.

b) Fixed-wing test design: The lift and drag coefficients of the wings are measured when they are statically fixed in water flow of constant speeds. As explained in the previous section, C_L and C_D are functions of AoA, which can vary with the Reynolds number (Re). The Reynolds number is defined by $\mathrm{Re} = |\boldsymbol{v}_{in}|c_g/\nu$, where $\boldsymbol{v}_{in}$ represents the inflow velocity, c_g is the geometric mean chord of the wing and ν is the kinematic viscosity of the fluid. To vary the Re number of a certain wing model, we control the inflow velocity and kinematic viscosity by adjusting the flow velocity $\boldsymbol{U}$ and water temperature T in the water tunnel, respectively. As listed in Table 2, we set two conditions of the water flow to obtain a comparatively low (condition 1) and a comparatively high (condition 2) Reynolds number for each sweepback wing. For water temperatures of 25°C, the density is 997.075 kg/m^3, and the kinematic viscosity is 0.8928 mm^2/s; for a water temperature of 40°C, the density is 992.247 kg/m^3, and the kinematic viscosity is 0.6578 mm^2/s [31]. In the two test conditions, the Re number for condition 1 is close to that of a penguin in an aquarium when swimming at less than 0.5 m/s (between 15000 and 30000); the Re number for condition 2 is close to that of a penguin in an aquarium when swimming between 0.5 m/s and 1 m/s (between 70000 and 96000) [20]. The method of calculating C_L and C_D is based on Equations (3) and (4). The rotation stage is used to vary the AoA of the wing. All the measurements are repeated three times, and time-averaged data of five seconds in each trial are used for calculating the C_L and C_D.

Table 2. REYNOLDS NUMBERS IN FIXED-WING TESTS

Sweepback angle (°)	**Reynolds number**	
	Condition 1 T: 25℃, U: 1.2 m/s	**Condition 2** T: 40℃, U: 2 m/s
0	29977	67785
10	30649	69305
20	31859	72040
30	34817	78728
40	39387	89063
50	46646	105477

c) Flapping-wing test design: To study the flapping-wing performance, we measure the thrust when different sweepback wing models are actuated to follow various flapping motions. Based on our measurement of real penguins [19], the flapping and feathering motions are defined by

$$\theta_{flap} = A_{flap}\sin(2\pi ft) \qquad (6),$$

$$\theta_{feather} = A_{feather}\sin(2\pi ft - \pi/2) \qquad (7),$$

where A_{flap} and $A_{feather}$ are the amplitudes and f represents the frequency. $A_{feather}$ is set to 0°, 10°, 20°, 30°, and 40°. Other hydrodynamic parameters are summarized in Table 3, where three trial sets are specified.

In trial set 1, different sweepback wings are actuated by the same motion (i.e., A_{flap} and f). In this set, the larger sweepback angle leads to a smaller flapping velocity $|\boldsymbol{v}_{flap}|$ due to the shorter spanwise widths, resulting in a smaller Strouhal number (St). The St number is defined as $\mathrm{St} = fL_{arc}/|\boldsymbol{U}|$, where f is the flapping frequency, L_{arc} is the arc length of the wing tip during flapping motion and $\boldsymbol{U}$ is the flow velocity. The flapping velocity $|\boldsymbol{v}_{flap}|$ can be calculated as follows:

$$\left|\boldsymbol{v}_{flap}\right| = 0.75 l' \cdot \omega_{flap} \quad (8),$$

where l' is the spanwise width and ω_{flap} is the angular velocity of the flapping motion.

To compare different sweepback angles with the same St number, trial sets 2 and 3 are employed. In trial set 2, A_{flap} is constant, while f is adjusted to achieve the target St number. In trial set 3, f is constant, while A_{flap} is adjusted for each St number. Both trial sets are conducted to investigate the effect of f and A_{flap} on thrust performance even under the same St number. The resultant Re and 1/St values are provided in Fig. 5 and Table 3. The Re number is defined as the maximum value at the mid-stroke when the inflow velocity $\boldsymbol{v}_{in}$ is maximized. It is seen through the Re that the high flow speed situations are more similar to aquarium penguins when they swim between 0.83 m/s and 1.12 m/s, as we studied before (corresponding to Re numbers from 7×10^4 to 11.1×10^4) [19]. Moreover, a higher flow speed also leads to a smaller St number, which ranges from approximately 0.6 to 0.2, as in aquarium penguins [19]. The literature has shown that many flying and swimming animals cruise in this range of St numbers for high locomotion efficiency as well [32].

In all measurements of the flapping wing, the rotation stage is fixed in the initial position. All the trials are repeated five times, and in each trial, the wing mechanism is actuated to flap 20 times, and only the force data from the middle 10 times are recorded.

In this paper, we focus on the thrust generated in the forward swimming direction (F_X). The net thrust N_X is employed for evaluating the propulsion ability, which can be calculated by $N_x = f/10 \int_0^{10/f} F_x(t)dt$, where $10/f$ denotes the duration of 10 flaps.

Table 3. PARAMETER SETTINGS IN FLAPPING-WING TESTS

Description	**Trial Set 1: constant A_{flap} and f**						**Trial Set 2: constant St and A_{flap}**					
Sweep (°)	0	10	20	30	40	50	0	10	20	30	40	50
T (°C)	40						40					
U (m/s)	0, 0.4, 0.8, 1.2, 1.6						0, 0.4, 0.8, 1.2, 1.6					
A_{flap} (°)	45						45					
f (Hz)	2.5						1.6	1.64	1.7	1.87	2.1	2.5
Maximum Re ($\times 10^4$) for each U	3.2, 3.4, 4.2, 5.2, 6.3	3.2, 3.5, 4.2, 5.2, 6.4	3.2, 3.5, 4.3, 5.4, 6.6	3.2, 3.5, 4.5, 5.7, 7.1	3.2, 3.6, 4.8, 6.2, 7.8	3.2, 3.8, 5.3, 7.1, 9.0	2.0, 2.4, 3.4, 4.5, 5.8	2.1, 2.5, 3.5, 4.7, 5.9	2.2, 2.6, 3.6, 4.8, 6.2	2.4, 2.8, 3.9, 5.3, 6.7	2.7, 3.2, 4.5, 6.0, 7.6	3.2, 3.8, 5.3, 7.1, 9.0
1/St for each U	0, 1.01, 2, 3.03, 4	0, 1.03, 2.04, 3.13, 4.17	0, 1.08, 2.13, 3.23, 4.35	0, 1.18, 2.33, 3.45, 4.76	0, 1.32, 2.63, 4, 5.26	0, 1.56, 3.13, 4.76, 6.25	0, 1.56, 3.13, 4.76, 6.25	0, 1.56, 3.13, 4.76, 6.25	0, 1.56, 3.13, 4.76, 6.25	0, 1.56, 3.13, 4.76, 6.25	0, 1.56, 3.13, 4.76, 6.25	0, 1.56, 3.13, 4.76, 6.25
St for each U	∞, 0.99, 0.50, 0.33, 0.25	∞, 0.97, 0.49, 0.32, 0.24	∞, 0.93, 0.47, 0.31, 0.23	∞, 0.85, 0.43, 0.29, 0.21	∞, 0.76, 0.38, 0.25, 0.19	∞, 0.64, 0.32, 0.21, 0.16	∞, 0.64, 0.32, 0.21, 0.16	∞, 0.64, 0.32, 0.21, 0.16	∞, 0.64, 0.32, 0.21, 0.16	∞, 0.64, 0.32, 0.21, 0.16	∞, 0.64, 0.32, 0.21, 0.16	∞, 0.64, 0.32, 0.21, 0.16

	Trial Set 3: constant St and f

Sweep (°)	0	10	20	30	40	50
T (°C)	40					
U (m/s)	0, 0.4, 0.8, 1.2, 1.6					
A_{flap} (°)	29	29.6	30.9	33.7	38.1	45
f (Hz)	2.5					
Maximum Re ($\times 10^4$) for each U	2.0, 2.4, 3.4, 4.5, 5.8	2.1, 2.5, 3.5, 4.7, 5.9	2.2, 2.6, 3.6, 4.8, 6.2	2.4, 2.8, 3.9, 5.3, 6.7	2.7, 3.2, 4.5, 6.0, 7.6	3.2, 3.8, 5.3, 7.1, 9.0
1/St for each *U*	0, 1.56, 3.13, 4.76, 6.25	0, 1.56, 3.13, 4.76, 6.25	0, 1.56, 3.13, 4.76, 6.25	0, 1.56, 3.13, 4.76, 6.25	0, 1.56, 3.13, 4.76, 6.25	0, 1.56, 3.13, 4.76, 6.25
St for each *U*	∞, 0.64, 0.32, 0.21, 0.16	∞, 0.64, 0.32, 0.21, 0.16	∞, 0.64, 0.32, 0.21, 0.16	∞, 0.64, 0.32, 0.21, 0.16	∞, 0.64, 0.32, 0.21, 0.16	∞, 0.64, 0.32, 0.21, 0.16

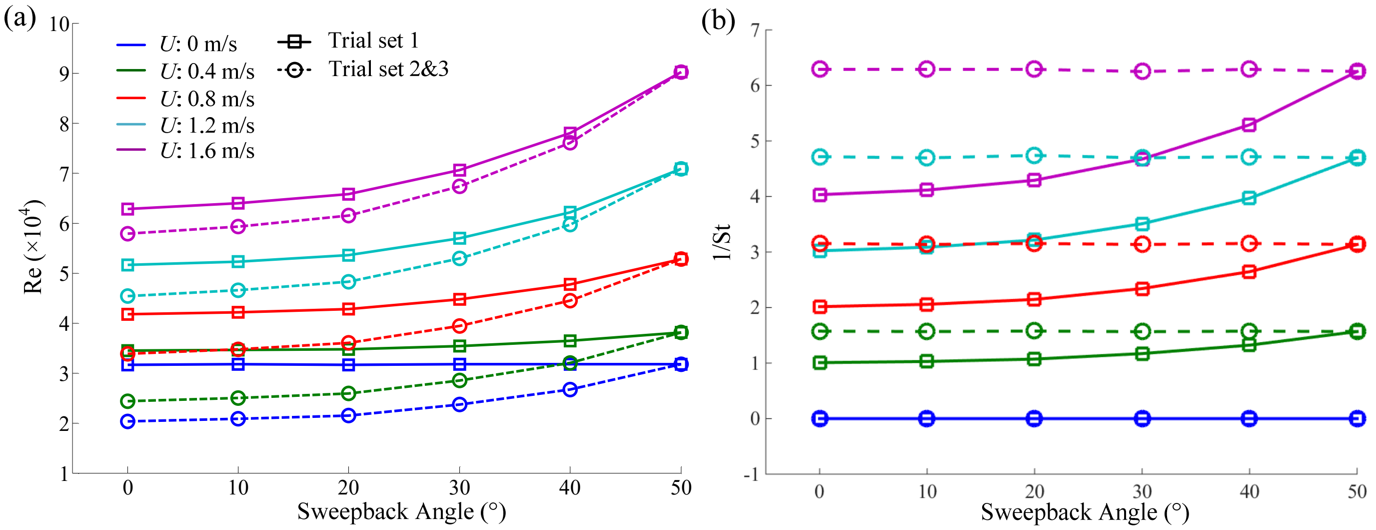

Fig. 5. Resultant (a) Reynolds number Re and (b) 1/St in flapping-wing tests.

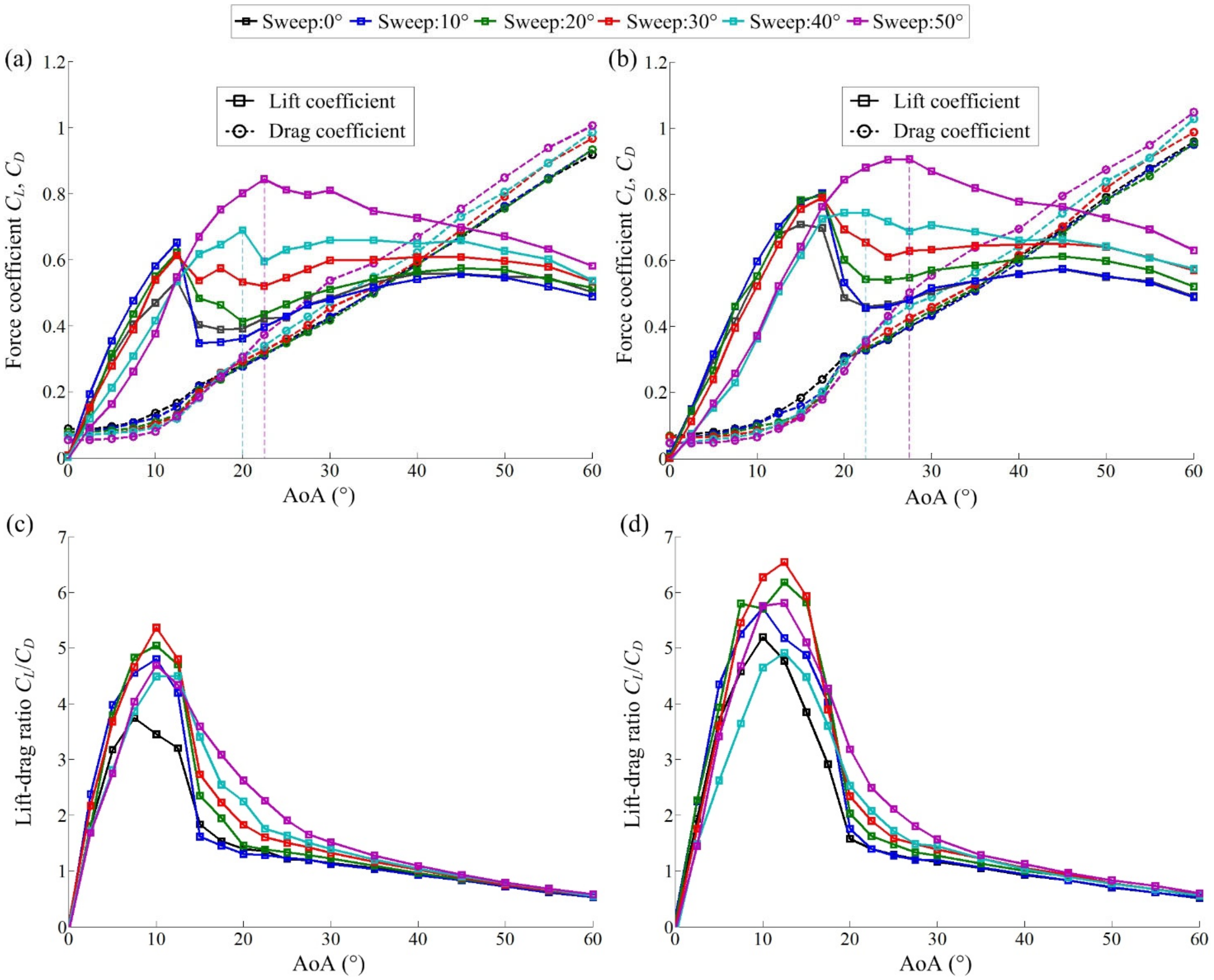

Fig. 6. Lift and drag coefficients C_L and C_D of (a) low Re (from 3.0×10^4 to 4.7×10^4), corresponding to test condition 1 in Table II, and (b) high Re (from 6.8×10^4 to 10.5×10^4), corresponding to test condition 2; lift-to-drag ratio C_L/C_D of (c) the low-Re condition and (d) the high-Re condition.

3. Results

3.1. Lift and drag coefficients in the fixed-wing test

The lift and drag coefficients of all the sweepback wings for the fixed-wing tests are shown in Fig. 6(a)(b), where Fig. 6(a) and Fig. 6(b) correspond to test condition 1 (low Re) and test condition 2 (high Re), respectively, which are listed in Table 2. Initially, all lift coefficients C_L increase with increasing AoA. Then, the C_L curves reach extreme values and start to drop. We refer to this extreme AoA angle as the stall angle in this paper.

A comparison of the wings of different sweepback angles indicates that the wings of large sweepback angles (i.e., 40° and 50°) produced gentler lift slopes before stalls for both low and high Re numbers (Fig. 6(a)(b)). The stall angles are accordingly postponed as well, being 20° and 22.5° for sweepback angles of 40° and 50° at low Re numbers and 22.5° and 27.5° for sweepback angles of 40° and 50° at high Re numbers, respectively (marked with dotted lines). Moreover, the decrease in C_L after the stall angle for large sweepback angles is gentle at both low and high Re numbers, while it is abrupt for small sweepback angles (i.e., from 0° to 30°). Note that in aerodynamics, a wing with a high AR leads to a steeper lift slope, while a wing with a low AR leads to a gentler lift slope with increasing stall angle, preventing flow separation [33]. Based on our wings' AR values in Table 1, we assume that sweepback angles from 0° to 30° correspond to larger-AR wings, while sweepback angles larger than 40° correspond to small Ars. A comparison of Fig. 6(a) and (b) indicates that the increase in the Re number also delays stalling and increases the maximum C_L for all sweepback angles, which is more prominent for small sweepback angles. Note that our previous CFD simulation of the same 3-D scanned wing without symmetrisation also shows that the stall angle is delayed by an increase in Re [23].

For the drag coefficient C_D, a larger sweepback angle leads to a smaller C_D before the stall for both low and high Re numbers. After the stall, a larger sweepback angle leads to a higher C_D, similar to the case of C_L. The lift-to-drag ratio, C_L/C_D, is shown in Fig. 6(d). The maximum lift-to-drag ratio also increases with an increasing Re number. Among the different sweepback angles, the sweepback angle of 30° produces the largest lift-to-drag ratio for both low and high Re numbers. After the stall, the larger sweepback angle achieves a larger lift-to-drag ratio.

In summary, the wing characteristics of a large sweepback angle (i.e., 40° and 50°) are favourable in terms of the large stall angle, large maximum C_L, moderate drop of the C_L curve after a stall, and low sensitivity to the Re number. On the other hand, a small sweepback angle (i.e., 10°, 20°, 30°) is preferred in terms of a high lift-to-drag ratio before a stall. Note that the 0° sweepback wing seems not to follow the above trend because its lift slope is not steep and the maximum lift-to-drag ratio is not large even with a high AR. This may be due to the curvature of the leading edge, which makes the leading edge advance rather than sweep back at the proximal region.

3.2. Thrust in the flapping-wing test

a) Thrust generation during a flapping cycle: Fig. 7(a) shows an example of the measured angular positions in one period, where A_{flap} =45°, $A_{feather}$ =10°, and $|\boldsymbol{U}|$ =0.8 m/s. The upstroke and downstroke are distinguished by white and grey backgrounds, respectively. The AoA is calculated based on (2). The phase of AoA is synchronized with that of the feathering angle. According to (2), the AoA is dependent on the feathering angle $\theta_{feather}$ and the flow velocity $\boldsymbol{U}$. For clarity, Fig. 7(b) shows the AoA curves for two different feathering amplitudes and two flow speeds, distinguishing sweepback angles of 0° and 30°. The AoA amplitude decreases with increasing flow velocity and feathering amplitude. In addition, the AoA amplitudes of the sweepback wing model are always several degrees smaller than those of the no-sweepback wing. Concerning the reasons, it is shown in Table 1 that the sweepback wing model has a shorter spanwise width l_0 due to the constant wing length l. Thus, the flapping velocity $|\boldsymbol{v}_{flap}|$ in Fig. 3(b) and (2) is comparatively smaller for the AoA.

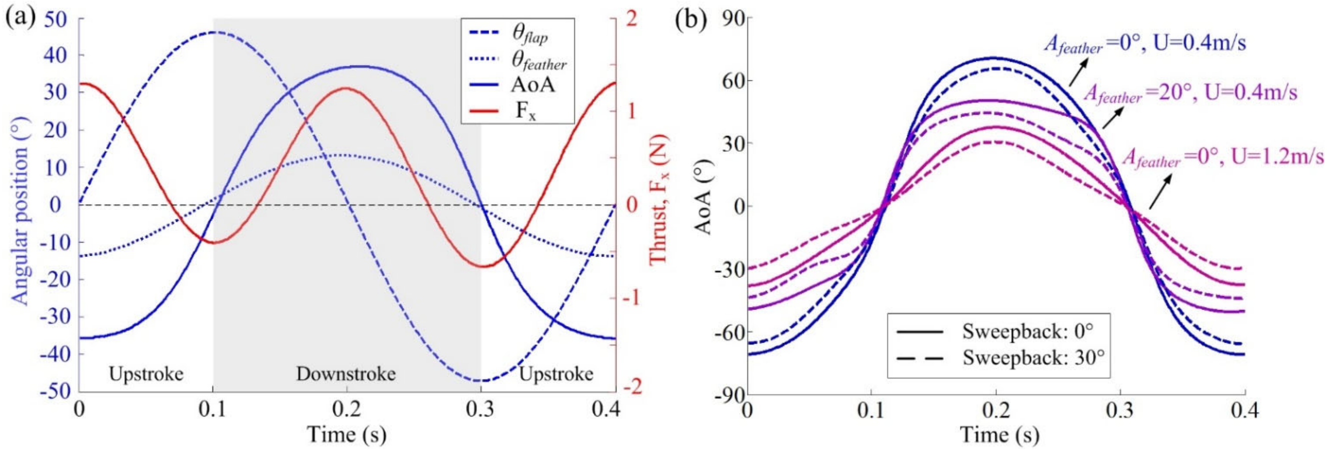

Fig. 7. (a) Actual angular positions of the wing with a sweepback angle of 30° in one period when flapping with a feathering amplitude of 10° at a flow speed of 0.8 m/s and the generated thrust; (b) AoA of two wing models in one period varying with different feathering amplitudes and flow speeds.

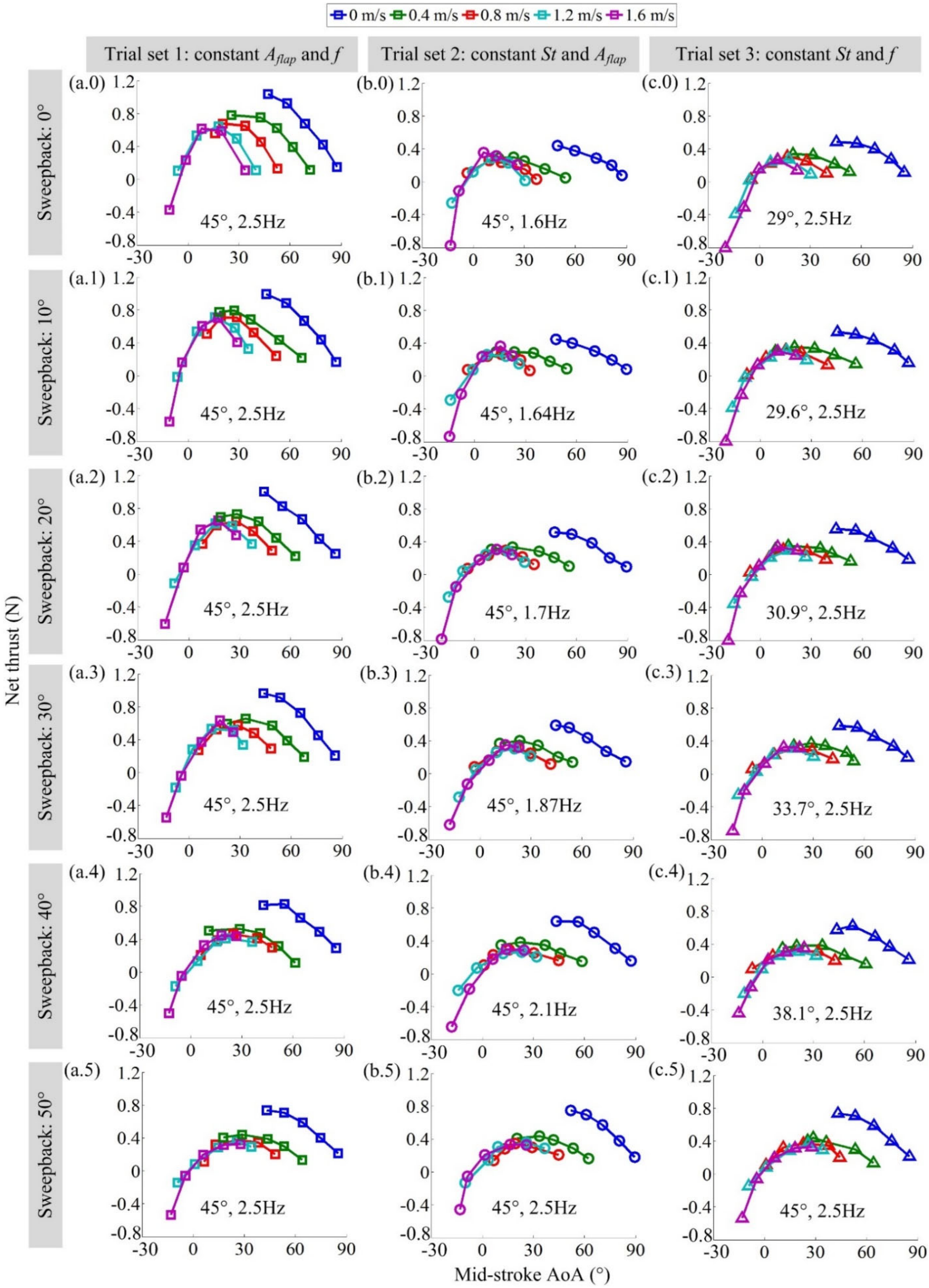

Fig. 8. Net thrusts generated by the wing mechanism at various flow speeds and flapping motions. Three columns indicate three trial sets, and five rows indicate wings with sweepback angles from 0° to 50°. A larger $A_{feather}$ leads to a smaller mid-stroke AoA.

Fig. 7(a) also depicts the instantaneous thrust F_x produced in one period. The flapping wing generates positive thrust near the mid-stroke. The largest thrusts are found to be near 0 s, 0.2 s and 0.4 s, which correspond to large flapping velocities and large AoAs for large lifts. Lift is considered to be beneficial for generating effective thrusts. Conversely, negative thrusts exist near 0.1 s and 0.3 s, which correspond to the largest flapping angles θ_{flap} but smallest flapping velocities $|\boldsymbol{v}_{\boldsymbol{flap}}|$. As a result, the AoA is almost zero, and the forces applied to the wing are mainly the drag generated by the water flow. Hence, the thrusts are measured to be negative near these two moments.

b) Net thrust per flapping cycle: The net thrust N_x is shown in Fig. 8, where subfigures (a), (b), and (c) indicate the three trial sets listed in Table 3, and from subfigures (a.0) to (a.5), sweepback angles from 0° to 50° correspond one-to-one. The flapping amplitude and frequency are marked in each subfigure as well. The net thrust generally increases with increasing AoA before an extreme point, after which the thrust starts to decrease. However, the extreme point might not occur for the low flow speed situation (i.e., 0 m/s) due to the large AoAs even with the maximum feathering amplitude of 40°. Note that the maximum feathering amplitude is limited by the rotational speed of the motors.

Comparing different trial sets, we see that trial set 1 generates larger net thrusts due to the larger flapping amplitude and frequency when the sweepback angle is small. The effect is prominent when the sweepback angle is less than 40°. However, the net thrust differences between trial sets 2 and 3 are very small, which indicates that the wings generate practically the same thrust when given the same St number, regardless of whether the flapping amplitude or the frequency is varied. Among different sweepback angles, the net thrust decreases with larger sweepback when flapping with the same amplitude and frequency (as shown in Fig. 8(a) trial set 1) because the larger sweepback results in a shorter spanwise width l' and a smaller flapping velocity $|\boldsymbol{v}_{\boldsymbol{flap}}|$. This is also the reason we designed trial sets 2 and 3 on the basis of the same St number. The net thrust does not change much at different sweepback angles, as shown in Fig. 8(b)(c).

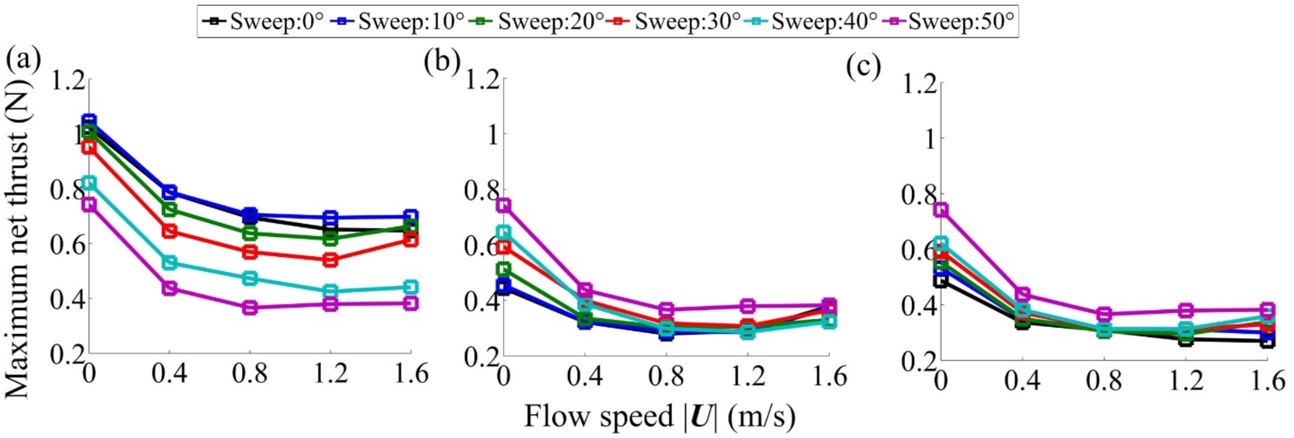

Fig. 9. Maximum net thrusts that can be generated by various sweepback flapping wings at different swimming velocities: (a) Trial set 1, same A_{flap} and f; (b) Trial set 2, same St and A_{flap}; (c) Trial set 3, same St and f.

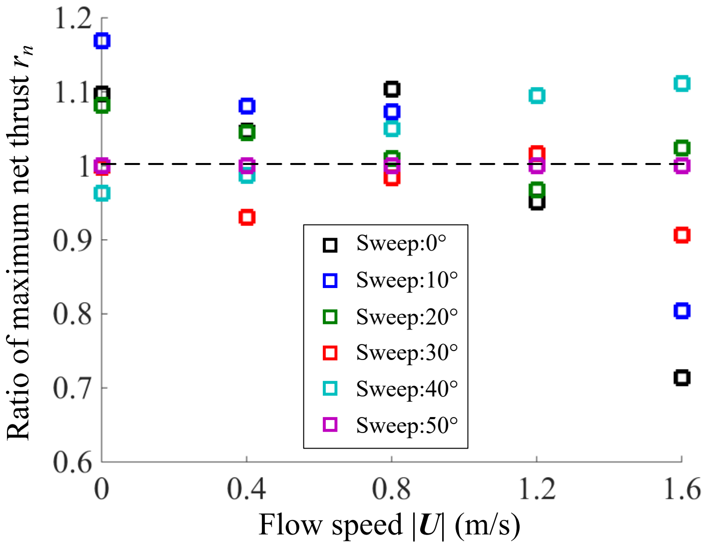

Fig. 10. Ratio of the maximum net thrust of set 3 to that of set 2.

To quantify the effect of sweepback on the net thrust more clearly, we depict the maximum net thrusts achieved by the optimal feathering amplitude for each flow speed in Fig. 9. The maximum net thrust decreases with increasing flow speeds and tends to be constant after 0.8 m/s in all trial sets. If comparing the thrust magnitudes in Fig. 9(a) of trial set 1, we notice that smaller sweepback angles are more beneficial for generating larger maximum net thrusts than larger sweepback angles. Note that the flapping velocity $|\boldsymbol{v}_{flap}|$ in the less-sweepback wing is larger than that in the larger-sweepback wing due to the larger spanwise width l', resulting in a larger inflow velocity $|\boldsymbol{v}_{in}|$ (Fig. 3(b)). According to Eqs. (3) and (4), the hydrodynamic forces are proportional to the square of the inflow velocity. Thus, wings with smaller sweepback angles generate larger maximum net thrusts.

To compensate for the difference in the inflow velocity resulting from sweepback angles, trial sets 2 and 3 are designed as illustrated in subsection 2.4 (c). The results are shown in Fig. 9(b)(c), where the wings with larger sweepback angles generate larger thrusts under the same St number for both trial sets. In particular, the largest sweepback angle of 50° is notable. Moreover, trial set 3 produces more net thrust than trial set 2 when the sweepback is small (i.e., 0°, 10°, 20°) and the flow velocity is low (i.e., 0 m/s), while trial set 2 produces more net thrust with a small sweepback angle at a high flow velocity (i.e., 1.6 m/s). The ratio of the maximum net thrust (r_n) of trial set 3 to that of trial set 2 in Fig. 10 also proves this.

c) Variation in thrust within a flapping cycle: To more thoroughly inspect the difference between trial sets 2 and 3, the variation in thrust within a flapping cycle is compared for the cases of the maximum net thrust.

The time variation in the thrusts within a flapping cycle is similar to that in Fig. 7(a). Therefore, we depict the instantaneous maximum and minimum values of the thrust within a flapping cycle for each case of the maximum net thrust, as shown in Fig. 11. Trial set 3 is found to generate larger absolute values of the maximum and minimum thrusts than trial set 2 in most situations, leading to larger variations in thrusts within a flapping cycle. That is, given the same St number, the combination of a small flapping amplitude A_{flap} and high frequency f (represented by trial set 3) can result in a large instantaneous thrust but is accompanied by a large instantaneous negative thrust. On the other hand, the combination of large A_{flap} and small f (represented by trail set 2) can achieve stable propulsions with less thrust fluctuation within a flapping cycle.

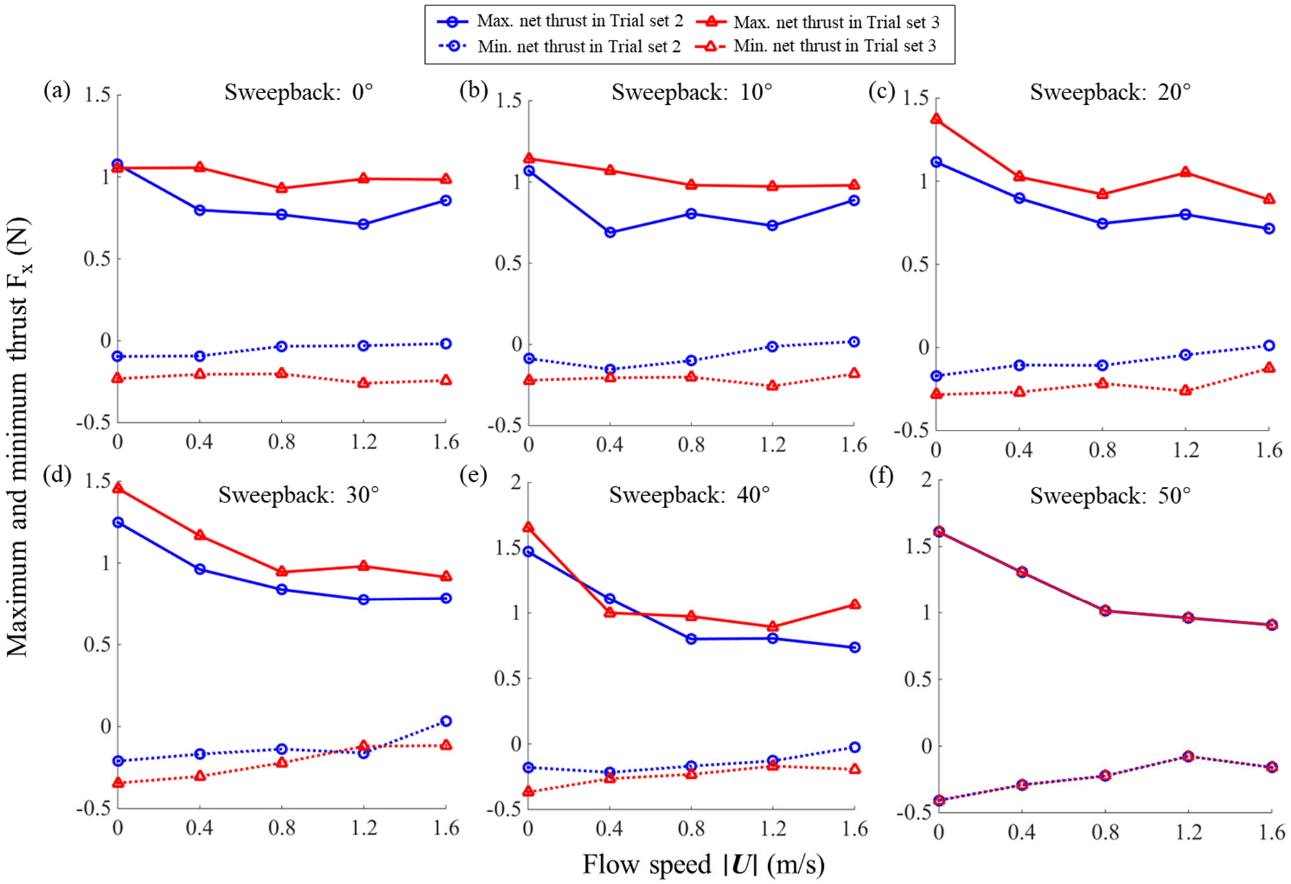

Fig. 11. Comparison of the maximum and minimum thrusts generated with the same St but different kinematics. Blue curves indicate a larger A_{flap} and smaller f in Trial set 2, and red curves indicate a smaller A_{flap} and larger f in Trial set 3. Sweepback angle changes from (a) 0° to (f) 50°.

d) Optimal AoA amplitude for the maximum net thrust: The optimal AoA amplitude for the maximum net thrust tends to be larger when the sweepback angle is large, as shown in Fig. 12. Data for the 0 m/s flow speed are eliminated from Fig. 12 since the maximum net thrust may not be realized (Fig. 8) due to feathering angle limitations. Most of the optimal AoA amplitudes fall within the range from 10° to 30°. The mean values of the optimal AoA amplitudes at each flow velocity are also shown. As illustrated in Section IV. A, we approximately classify the sweepback angle into large sweepback angles (i.e., 40°, 50°) and small sweepback angles (i.e., 0°, 10°, 20°, 30°) based on the lift coefficients. Hence, the mean values include those of all sweepback angles. The optimal AoA amplitude tends to decrease with increasing flow velocity. Moreover, the larger-sweepback wings are associated with larger optimal AoA amplitudes, which means they need less feathering motion to achieve the maximum net thrust.

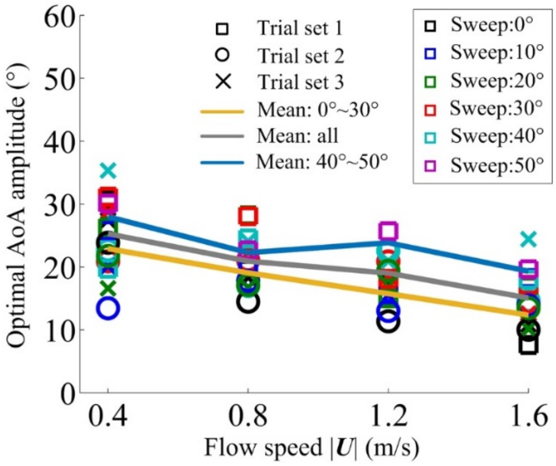

Fig. 12. Optimal AoA amplitudes when maximum net thrusts are achieved in all the wings and the mean values.

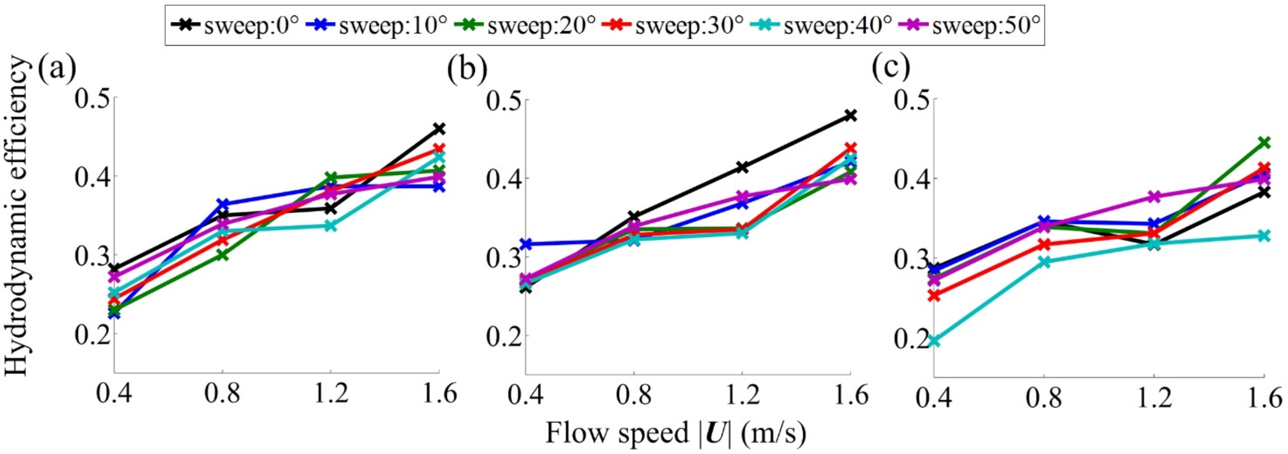

Fig. 13. Hydrodynamic efficiency for the maximum net thrust with various sweepback wings at different swimming velocities. (a) Trial set 1: same A_{flap} and *f* for each flow speed. (b) Trial set 2: same St and A_{flap} for each flow speed. (c) Trial set 3: same St and *f* for each flow speed.

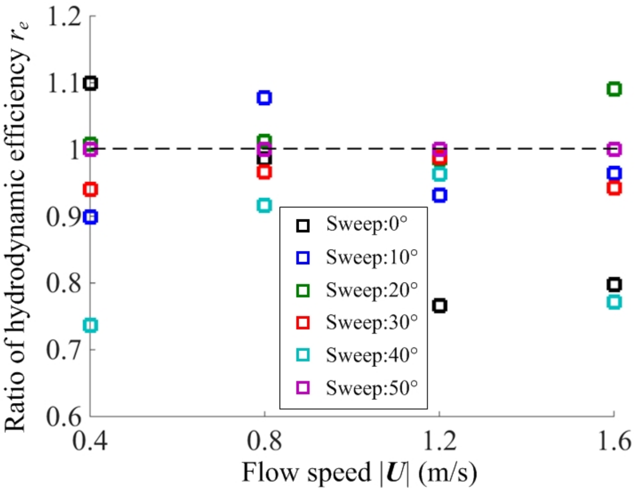

Fig. 14. Hydrodynamic efficiency ratio of Trial set 3 to Trial set 2.

3.3. Hydrodynamic efficiency

The hydrodynamic efficiency for the maximum net thrust cases is shown in Fig. 13. For all trial sets, the efficiency increases with increasing flow speed, although a clear trend for the sweepback is not found. Even for the same St number, which is subject to trial sets 2 and 3 (Fig. 12(b)(c)), a clear relationship between the sweepback and efficiency is not found. The ratio of the efficiency (r_e) of trial set 3 to trial set 2 is calculated and shown in Fig. 14 for reference. In conjunction with the results of the net thrust per flapping cycle (Fig. 9), the analysis indicates that the penguin wing can generate large thrust with low efficiency at slow swimming speeds and can achieve high efficiency with less thrust at high swimming speeds. Note that the relationship between the efficiency and sweepback for constant cruising with less thrust demand is still unknown.

4. Conclusion

In this paper, an electric penguin-mimetic wing mechanism was applied to investigate the effect of wing sweepback on thrust generation. Five alternative wing models with different sweepback angles were prepared for comparison. To understand the static wing characteristics in steady flow, the lift and drag coefficients of the wings were first measured in a water tunnel in a statically fixed scenario. Among the studied sweepback angles, small-sweepback wings (from 0° to 30°, AR>3) were found to have steeper lift curves, while the large-sweepback wings (from 40° to 50°, AR<3) increased the stall angle and could maintain lift after a stall, which implies robustness of the large sweepback to variation in the AoA. In addition, a moderate sweepback angle (30°, AR=3.4) was verified to have the largest lift-to-drag ratio in steady flow.

Then, the thrust during wing flapping was measured. With a larger feathering amplitude, the AoA amplitude decreased, and the thrust increased before the stall point. Concerning the maximum net thrust, smaller-sweepback wings were found to generate larger thrusts if following the same wing motion, benefiting from longer spanwise widths. However, at the same St number, larger sweepback wings could generate more thrust. The optimal AoA amplitudes for realizing the maximum thrust tended to decrease with increasing flow speed. Finally, the hydrodynamic efficiency of propulsion with flapping was evaluated. The efficiency for the maximum net thrust increased with increasing flow speed, while a clear relationship with the sweepback angle was not found.

Overall, the sweepback of the wing decreased the net thrust given the same wing motion and increased the net thrust given the same St number. The effect of the sweepback on the propulsion efficiency for the maximum net thrust was not clear. This paper presented an experimental verification of the sweepback effect based on preset conditions, which is also the basis for realizing motion control of a penguin-mimetic swimming robot. In future studies, we plan to investigate the effect of wing flexibility and passive deformation on thrust performance and structural requirements.

Funding. This work was supported by the JSPS KAKENHI Grant-in-Aid for Scientific Research on Innovative Areas "Science of Soft Robot" Project under Grant JP18H05468.

Acknowledgements. All experiments and measurements were conducted at the Tokyo Institute of Technology.

References

[1] F.E. Fish, Advantages of aquatic animals as models for bio-inspired drones over present AUV technology, Bioinspiration & biomimetics, vol. 15, no. 2, 025001, 2020.

[2] A. Raj and A. Thakur, "Fish-inspired robots: design, sensing, actuation, and autonomy—a review of research," Bioinspiration & biomimetics, vol. 11, no. 3, 031001, 2016.

[3] J. E. Colgate and K. M. Lynch, "Mechanics and control of swimming: A review," IEEE journal of oceanic engineering, vol. 29, no. 3, pp. 660–673, 2004.

[4] W.-S. Chu, K.-T. Lee, S.-H. Song, M.-W. Han, J.-Y. Lee, H.-S. Kim, M.-S. Kim, Y.-J. Park, K.-J. Cho, and S.-H. Ahn, "Review of biomimetic underwater robots using smart actuators," International journal of precision engineering and manufacturing, vol. 13, no. 7, pp. 1281–1292, 2012.

[5] A. Jaya, M. Kartidjo, “Thrust and efficiency enhancement scheme of the fin propulsion of the biomimetic Autonomous Underwater Vehicle model in low-speed flow regime,” Ocean Engineering, 243: 110090, 2022.

[6] K. Kikuchi, Y. Uehara, Y. Kubota, and O. Mochizuki, “Morphological considerations of fish fin shape on thrust generation.” Journal of Applied Fluid Mechanics, vol. 7, no. 4, pp. 625-632, 2014.

[7] K. L. Feilich and G. V. Lauder, “Passive mechanical models of fish caudal fins: effects of shape and stiffness on self-propulsion,” Bioinspiration & biomimetics, vol. 10, no. 3, 036002, 2015.

[8] K. N. Lucas, P. J. Thornycroft, B. J. Gemmell, S. P. Colin, J. H. Costello, and G. V. Lauder, “Effects of non-uniform stiffness on the swimming performance of a passively-flexing, fish-like foil model,” Bioinspiration & biomimetics, vol. 10, no. 5, 056019, 2015.

[9] Q. Zhong, J. Zhu, F.E. Fish, S.J. Kerr, A.M. Downs, H. Bart-Smith, and D.B. Quinn, “Tunable stiffness enables fast and efficient swimming in fish-like robots,” Science Robotics, 6(57): eabe4088, 2021.

[10] Y.-J. Park, T. M. Huh, D. Park, and K.-J. Cho, “Design of a variable stiffness flapping mechanism for maximizing the thrust of a bioinspired underwater robot,” Bioinspiration & biomimetics, vol. 9, no. 3, 036002, 2014.

[11] D. B. Quinn, G. V. Lauder, and A. J. Smits, “Maximizing the efficiency of a flexible propulsor using experimental optimization,” Journal of Fluid Mechanics, vol. 767, pp. 430–448, 2015.

[12] C. Eloy, “On the best design for undulatory swimming,” Journal of Fluid Mechanics, vol. 717, pp. 48–89, 2013.

[13] H. Park, Y.-J. Park, B. Lee, K.-J. Cho, and H. Choi, “Vortical structures around a flexible oscillating panel for maximum thrust in a quiescent fluid,” Journal of Fluids and Structures, vol. 67, pp. 241–260, 2016.

[14] Y. Liu, H. Li, S. Deng, S. Wang, S. Liu, and Z. Wang, “Biomimetic Robotic Sea Lion Foreflippers: Design, Modeling, and Experimentation,” IEEE/ASME Transactions on Mechatronics, vol. 27, no. 6, pp. 5679–5689, 2022.

[15] B. Kwak, D. Lee, J. Bae, “Comprehensive analysis of efficient swimming using articulated legs fringed with flexible appendages inspired by a water beetle,” Bioinspiration & biomimetics, vol. 14, no. 6, 066003, 2019.

[16] Y. Shen, H. Pu, and S. Ma, “Realizing efficient front crawl stroke with a wheel-paddle-integrated mechanism: Inspired by human competitive swimming,” IEEE Journal of Oceanic Engineering, vol. 45, no. 3, pp. 831-839, 2019.

[17] J. M. Handley, A. Thiebault, A. Stanworth, D. Schutt, and P. Pistorius, “Behaviourally mediated predation avoidance in penguin prey: in situ evidence from animal-borne camera loggers,” Royal Society open science, vol. 5, no. 8, 171449, 2018.

[18] Mattern T, Pütz K, Garcia-Borboroglu P, Ellenberg U, Houston DM, Long R, et al, “Marathon penguins – Reasons and consequences of long-range dispersal in Fiordland penguins / Tawaki during the pre-moult period,” PLOS ONE, vol. 13, no. 8, e0198688, 2018.

[19] N. Harada, T. Oura, M. Maeda, Y. Shen, D. M. Kikuchi, and H. Tanaka, “Kinematics and hydrodynamics analyses of swimming penguins: wing bending improves propulsion performance,” Journal of Experimental Biology, vol. 224, jeb242140, 2021.

[20] Y. Shen, N. Harada, S. Katagiri, and H. Tanaka, “Biomimetic realization of a robotic penguin wing: Design and thrust characteristics,” IEEE/ASME Transactions on Mechatronics, vol. 26, no. 5, pp. 2350-2361, 2021.

[21] F.E. Fish, J.J. Rohr, “Review of dolphin hydrodynamics and swimming performance,” *Tech. Rep.* Space and Naval Warfare Systems Command, San Diego CA.10.21236/ADA369158, 1999.

[22] J. Yu, Z. Wu, Z. Su, T. Wang, and S. Qi, “Motion control strategies for a repetitive leaping robotic dolphin,” IEEE/ASME Transactions on Mechatronics, vol. 24, no. 3, pp. 913–923, 2019.

[23] M. Maeda, N. Harada, and H. Tanaka, “Hydrodynamics of gliding penguin flipper suggests the adjustment of sweepback with swimming speeds,” bioRxiv, 2021.

[24] R. Russo, S. Blemker, F. Fish, and H. Bart-Smith, “Biomechanical model of batoid (skates and rays) pectoral fins predicts the influence of skeletal structure on fin kinematics: implications for bio-inspired design,” Bioinspiration & biomimetics, vol. 10, no. 4, 046002, 2015.

[25] R. G. Bas, W. Serra, R. Trinchin, V. Leoni, L. Rubio, L. Sampognaro, G. Nagy, A. Cravino, and A. Acu˜na, “Confirmation of mola mola (tetraodontiformes: Molidae) and historical records of ocean sunfishes (mola sp.) in the coastal area of uruguay,” Marine Biodiversity Records, vol. 8, e21, 2015.

[26] A. R. Rivera, G. Rivera, and R. W. Blob, “Forelimb kinematics during swimming in the pig-nosed turtle, carettochelys insculpta, compared with other turtle taxa: rowing versus flapping, convergence versus intermediacy,” Journal of Experimental Biology, vol. 216, no. 4, pp. 668–680, 2013.

[27] T. Y. Hubel, N. I. Hristov, S. M. Swartz, and K. S. Breuer, “Wake structure and kinematics in two insectivorous bats,” Philosophical Transactions of the Royal Society B: Biological Sciences, vol. 371, no. 1704, 20150385, 2016.

[28] B. Klaassen van Oorschot, E. A. Mistick, and B. W. Tobalske, “Aerodynamic consequences of wing morphing during emulated takeoff and gliding in birds,” Journal of Experimental Biology, vol. 219, no. 19, pp. 3146–3154, 2016.

[29] A. N. Zurman-Nasution, B. Ganapathisubramani, and G. D. Weymouth, “Fin sweep angle does not determine flapping propulsive performance,” Journal of the Royal Society Interface, vol. 18, no. 178, 20210174, 2021.

[30] P. R. Bandyopadhyay, D. N. Beal, and A. Menozzi, “Biorobotic insights into how animals swim,” Journal of Experimental Biology, vol. 211, no. 2, pp. 206–214, 2008.

[31] J. Kestin, M. Sokolov, and W. A. Wakeham, “Viscosity of liquid water in the range- 8 c to 150 c,” Journal of Physical and Chemical Reference Data, vol. 7, no. 3, pp. 941–948, 1978.

[32] G. K. Taylor, R. L. Nudds, and A. L. Thomas, “Flying and swimming animals cruise at a strouhal number tuned for high power efficiency,” Nature, vol. 425, no. 6959, pp. 707–711, 2003.

[33] J.-M. Moschetta and C. Thipyopas, “Aerodynamic performance of a biplane micro air vehicle,” Journal of Aircraft, vol. 44, no. 1, pp. 291–299, 2007.